Vietnam Journal of Earth Sciences, 48(2), 277−298, https://doi.org/10.15625/2615-9783/24344

Vietnam Journal of Earth Sciences
https://vjs.ac.vn/index.php/jse

Monazite petrochronology constrains the metamorphic evolution of high-grade metamorphic rocks in the Dai Loc shear zone, Central Vietnam

Nam Nguyen Duc[1,3], Ching-Hua Lo[1], Tadashi Usuki[1], Yoshiyuki Iizuka[2], Mei-Fei Chu[1], Jian-Wei Lin[2], Pham Binh[3]

[1]*Department of Geosciences, National Taiwan University*
[2]*Institute of Earth Sciences, Academia Sinica, Nangang*
[3]*Vietnam Institute of Geosciences and Mineral Resources, Hanoi, Vietnam*

Received 29 September 2025; Received in revised form 29 February 2026; Accepted 16 March 2026

ABSTRACT

The Dai Loc shear zone in central Vietnam contains granulite-facies rocks and is a key area for studying the Early Paleozoic metamorphic evolution of the Indochina Block. An integrated study of in-situ geochronology, trace element geochemistry, and microtextural analysis was conducted to decipher the metamorphic evolution of this high-grade unit. Monazites from the two granulite samples display three distinct chemical domains, whose trace element compositions closely correlate with garnet growth and breakdown. Yttrium- and heavy rare-earth element (HREE)-rich monazite core domains are interpreted to have formed with limited garnet growth, recording a discrete growth episode during prograde metamorphism at ~435 Ma. Y- and HREE-poor domains are linked to significant garnet growth during peak conditions at ~420 Ma. The elevated Y+HREE concentrations in the outermost rim domains indicate their formation during garnet breakdown and likely date the retrograde metamorphism to ~390 Ma. These U–Pb monazite ages align well with the U-Pb zircon ages from granulites and syn-metamorphic granitoids in the study area, reinforcing the inferred metamorphic timeline. The results of this petrochronological study highlight the importance of integrating petrology with trace element data from major and accessory phases to link geochronological data to metamorphic *P–T* paths.

Keywords: Petrochronology, U-Pb geochronology, REE partitioning, garnet, monazite, restite, Indochina block.

1. Introduction

The majority of Southeast Asia comprises several Gondwana-derived fragments, including the Indochina, South China, and Sibumasu blocks (Fig. 1a). These continental blocks rifted from Gondwana and were subsequently accreted to Eurasia during the Paleozoic to Early Mesozoic (Metcalfe, 2006, 2013). The Indochina Block lies between the South China and Sibumasu Blocks, and its eastern domain forms a key tectonic segment consisting of the Kontum Massif (KTM) and the Truong Son Belt (TSB). Granulite-facies metamorphic rocks are widespread in the KTM (Nakano et al., 2004, 2007, 2013; Osanai et al., 2004; Roger et al., 2007; Bui et al., 2020). In contrast, within the TSB, such rocks are restricted to the Dai Loc shear zone (Bui et al., 2022; Nguyen et al., 2023). Previous studies suggest that granulite-facies

*Corresponding author, Email: dnamgeo@gmail.com

rocks exposed along the Dai Loc shear zone record two distinct tectono-metamorphic events (Nguyen et al., 2023). The first event is subdivided into three stages: prograde, peak, and retrograde, defining a tight clockwise metamorphic P–T path (Nguyen et al., 2023). Zircon geochronology indicates that this event occurred during the Early Paleozoic, but the timing of the individual metamorphic stages remains poorly constrained (Bui et al., 2022; Nguyen et al., 2023). The second event is defined by the development of fine-grained and mylonitic assemblages (Nguyen et al., 2023). Although direct geochronological evidence is absent, it has been suggested that this event occurred during the Triassic Indosinian orogeny (Nguyen et al., 2023). Consequently, the metamorphic evolution of the granulite-facies rocks in the TSB remains insufficiently resolved, and further petrochronological studies are required.

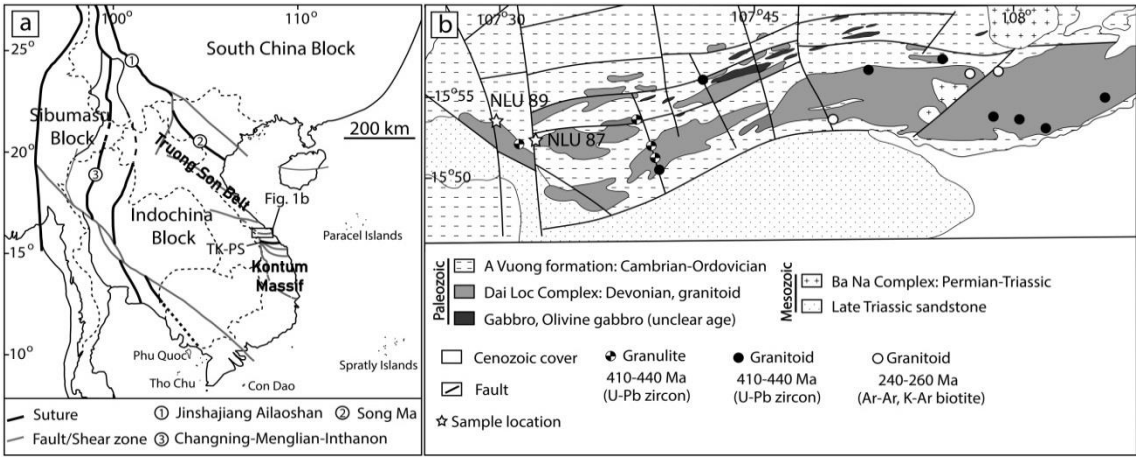

Figure 1. (a) Tectonic sketch map of SE Asia, modified after Metcalfe (2011) and Lepvrier et al. (2004). (b) Geological map of the Dai Loc shear zone with sample localities (Cat, 1996). Zircon U–Pb ages and mica Ar–Ar/K–Ar ages are from previous studies (Carter et al., 2001; Nguyen et al., 2023; Pham et al., 2016; Jiang et al., 2020; Lepvrier et al., 1997; Tran, 1998; Bui et al., 2022)

Understanding the pressure-temperature-time (*P–T–t*) path of metamorphism is crucial for unraveling the evolution of metamorphic complexes (Harley, 2016; Kelsey and Hand, 2015). It involves dating minerals that can be linked to specific metamorphic stages, a process known as petrochronology (Kohn et al., 2017). Aside from zircon, monazite is another commonly dated phase, typically found in metapelitic rocks with Ca-poor and Al-rich compositions, and grows over a wide range of metamorphic conditions (Catlos et al., 2002; Kohn et al., 2005; Skrzypek et al., 2017). Several studies have demonstrated that monazite can record multiple metamorphic stages/events and has proven to be a reliable accessory mineral for constraining the timing along the *P–T* path of polymetamorphic complexes (Hermann and Rubatto, 2003; Bhowmik et al., 2014; D'Souza et al., 2021; Petrík et al., 2019; Warren et al., 2019; Weller et al., 2020).

Although no explicit criteria directly link monazite ages to *P–T* paths, their formation can be correlated with the growth or breakdown of major minerals, such as garnet, through the analysis of textural relationships and chemical signatures between these phases (e.g., Dumond et al., 2015; Mottram et al., 2014). In high-grade metamorphic rocks, monazite included in garnet has been interpreted to form before or simultaneously

with garnet (Blereau et al., 2016; Mottram et al., 2014), whereas monazite in the matrix may crystallize from melts during cooling (Kelsey et al., 2008; Spear and Pyle, 2010). From a chemical perspective, the fractionation of Y between garnet and monazite has been successfully used to infer their relationship. Y-enriched monazite cores may have formed before significant garnet growth (e.g., Barnes et al., 2021; Benetti et al., 2024). Conversely, Y-poor monazite is generally interpreted to have formed coevally with or after a major garnet growth event (e.g., Sorger et al., 2024; Kohn et al., 2005). The breakdown of garnet via melt crystallization during cooling may have initiated the formation of high-Y monazite, which subsequently overgrew pre-existing monazite domains (e.g., Dumond et al., 2015; Kohn et al., 2005).

In this study, we present an integration of in situ U–Pb monazite dating, trace-element and microtextural analysis of granulite-facies rocks from the Dai Loc shear zone in central Vietnam (Fig. 1). The results reveal the timing of different metamorphic stages along the Early Paleozoic *P–T* path and highlight the behavior of monazite and garnet during these stages.

2. Geological background and samples

The Indochina Block is separated from the South China and Sibumasu Blocks by the Jinshajiang-Ailaoshan-Song Ma and Changning-Menglian-Inthanon sutures, respectively (Fig. 1a). Based on lithology, its eastern region is divided into two major tectonic units: the KTM and the TSB, which the Tam Ky separates-Phuoc Son (TK-PS) paleo-suture zone (Faure et al., 2018; Nguyen et al., 2019; Tran et al., 2014, 2020).

The KTM is considered the core of the Indochina Block (Fig. 1a). Its basement, which formed during the Paleoproterozoic and Mesoproterozoic (Lan et al., 2003), consists mainly of amphibolite- to granulite-facies rocks (Nakano et al., 2007; Osanai et al., 2004). Based on metamorphic grade, the massif is subdivided into the Kham Duc, Ngoc Linh, and Kannack complexes from north to south. The Kham Duc Complex records greenschist- to amphibolite-facies metamorphism under medium- to high-pressure conditions (Usuki et al., 2009; Nakano et al., 2009). In contrast, the Ngoc Linh and Kannack complexes consist mainly of high-pressure, high- to ultrahigh-temperature granulite-facies rocks (Nakano et al., 2004; Osanai et al., 2004; Roger et al., 2007). Two major tectonothermal events are recorded in these high-grade metamorphic rocks: the Ordovician-Silurian and Permian-Triassic events. Various dating methods have been applied to constrain the early Paleozoic tectonometamorphic evolution of the KTM (Bui et al., 2020; Nakano et al., 2013, 2021; Roger et al., 2007). The Ordovician-Silurian event occurred between 460 and 430 Ma, with prograde metamorphism at 450–440 Ma and a peak at ~430 Ma (Bui et al., 2020). This event has been attributed to subduction and subsequent collision between the KTM and the TSB (Usuki et al., 2009), collision between the Indochina and South China blocks (Faure et al., 2018; Gardner et al., 2017; Jiang et al., 2020; Ngo et al., 2022, 2025b; Tran et al., 2014; Wang et al., 2020), or arc-related magmatism (Nakano et al., 2013, 2021; Bui et al., 2022). The Permian-Triassic event, dated at ~260–240 Ma, is generally considered to have resulted from subduction and consequent collision between the Indochina and South China blocks during the Indosinian Orogeny (Faure et al., 2014; Nakano et al., 2010).

The South China Block bounds the TSB along the Song Ma suture zone to the north, and by the KTM along the TK-PS suture zone to the south (Lepvrier et al., 2004; Tran et al., 2014). Well-developed NW marks it-SE-trending shear zones (Fig. 1a; Lepvrier et al.,

1997, 2004, 2008). The TSB is predominantly composed of Neoproterozoic to Mesozoic volcano-sedimentary sequences that are intruded by numerous plutonic rocks of various ages (Burrett et al., 2021; Gardner et al., 2017; Pham et al., 2016; Ngo et al., 2025a; Jiang et al., 2020; Shi et al., 2015). Minor metamorphic rocks of greenschist-, amphibolite-, and granulite-facies conditions commonly occur along shear zones (Bui et al., 2022; Nguyen et al., 2023; Lepvrier et al., 2008).

The Dai Loc shear zone is a NW–SE-trending shear zone in the TSB, situated in its southern part and to the north of the TK–PS suture zone (Fig. 1a). Cenozoic volcano-sedimentary sequences characterize the eastern domain, whereas the western domain is dominated by Early Paleozoic rocks, including the A Vuong Formation, Dai Loc Complex, gabbro, and pelitic granulites (Fig. 1b; Bui et al., 2022; Nguyen et al., 2023; Cat, 1996). Permian–Triassic granitoids of the Ba Na complex were intruded locally along the shear zone (Fig. 1b). Detrital zircon U–Pb geochronology constrains the maximum depositional age of the A Vuong Formation to 516 Ma (Wang et al., 2016). Rocks of this formation underwent greenschist- to lower amphibolite-facies metamorphism with peak conditions of 5.5–8.7 kbar and 590–640°C (Bui et al., 2025).

Early Paleozoic igneous and granulite-facies metamorphic rocks are suggested to have been tectonically juxtaposed with the rocks of the A Vuong Formation during the Triassic (Nguyen et al., 2023). Previous studies have indicated that these high-grade metamorphic rocks experienced a polyphase metamorphic history (Nguyen et al., 2023). The earlier event occurred under granulite-facies conditions and was subdivided into prograde, peak, and retrograde stages. The prograde stage is represented by an inclusion assemblage of cordierite + sillimanite + biotite + quartz + spinel ± plagioclase, forming coarse-grained minerals, and occurred at 720–770°C and 5.8–6.4 kbar. Peak metamorphic conditions are recorded by a coarse-grained mineral assemblage of garnet + orthopyroxene + cordierite + plagioclase + K-feldspar + ilmenite + melt ± biotite in the matrix, with estimated conditions of 850–920°C and 5.3–6.3 kbar (Nguyen et al., 2023). The retrograde stage is characterized by symplectitic quartz + biotite replacing peritectic minerals, defining a near-isobaric cooling retrograde path (Nguyen et al., 2023). Zircon U–Pb geochronology of granulites and syn-metamorphic Dai Loc Complex yielded ages ranging from 440 to 410 Ma, which may represent the timing of post-peak metamorphism or the entire metamorphic cycle (prograde, peak, and retrograde; Bui et al., 2022; Nguyen et al., 2023). A post-collisional extensional tectonic setting has been proposed for the Early Paleozoic thermal event in the Dai Loc shear zone (Nguyen et al., 2023; Jiang et al., 2020). The later amphibolite-facies overprint is characterized by fine-grained mineral assemblages of kyanite + orthopyroxene + quartz + garnet + biotite + plagioclase + K-feldspar that pseudomorph coarse-grained phases. Peak amphibolite conditions were estimated at 600°C and 7.3 kbar (Nguyen et al., 2023) and are consistent with those estimated for rocks of the A Vuong Formation (Bui et al., 2025). Furthermore, the presence of a fine-grained kyanite-bearing assemblage in strongly deformed granitoids of the Dai Loc Complex is interpreted to have formed during this overprint (Nguyen et al., 2023). Therefore, Ar–Ar and K–Ar ages of 250–240 Ma obtained from synkinematic biotite and muscovite in rocks of the Dai Loc Complex likely record the timing of the amphibolite overprint (Tran et al., 1998; Lepvrier et al., 1997). This event may be related to subparallel dextral mylonitic shear associated

with the Triassic collision between the Indochina and South China blocks (Nguyen et al., 2023; Lepvrier et al., 1997).

Two granulite samples (NLU87 and NLU89) from different outcrops in the western part of the Dai Loc shear zone were selected for petrographic, chemical, and geochronological analyses (Fig. 2). At the outcrop scale, the rocks exhibit well-developed migmatitic structures characterized by alternating leucosome, mesosome, and restite domains. Leucosomes are widespread, occurring as patches or cm-scale layers subparallel to the regional foliation, suggesting partial melting and melt fractionation (Godet et al., 2010; Sawyer, 2008; Schorn and Diener, 2019). The restite domains occur as massive, dark-colored, garnet-rich layers (Fig. 2). Due to their abundance of monazite and their potential to preserve high-temperature metamorphic evolution (White and Powell, 2002), the collected samples were taken from restite domains.

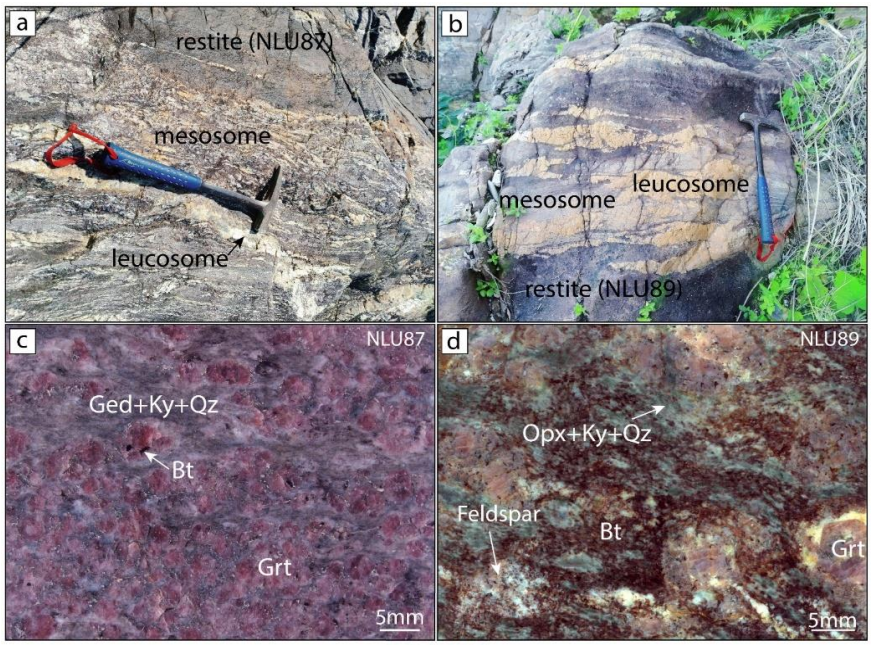

Figure 2. (a-b) Outcrop photographs of the studied samples in the Dai Loc shear zone. (c-d) Hand specimens of NLU87 and NLU89. The mineral abbreviations follow those of Whitney and Evans (2010)

3. Analytical Methods

3.1. Whole-rock analyses

Powdered representative samples were prepared using a jaw crusher and an agate ball mill. Major and REE element analyses of whole-rock samples (Table S1) were conducted by Australian Laboratory Services (ALS) Pty. Ltd. Details about the analytical procedure can be found in Nguyen et al. (2023) and on the ALS Global website (www.alsglobal.com).

3.2. Electron microprobe and Backscattered electron (BSE) image

Backscattered electron (BSE) imaging and electron microprobe analyses were conducted at the Institute of Earth Sciences, Academia Sinica, Taiwan, to identify monazite grains and to characterize internal textures and compositional domains in both monazite and garnet. Whole-section BSE images showing monazite localities are presented in Fig. S1. Individual monazite BSE images with

analyzed U–Pb and REE locations and elemental maps, as indicated in Fig. S1, are presented in Fig. S2. Detailed analytical conditions are provided in Appendix S1.

3.3. U–Pb dating and trace element analysis

U–LA conducted Pb geochronology and trace element analyses of monazite and garnet-ICP–MS at the Institute of Earth Sciences, Academia Sinica, Taiwan. Analytical spots were selected based on BSE images and X-ray elemental maps. U–Pb isotopic data and trace element compositions are presented in Tables S2 and S3. Full details of analytical procedures and conditions are provided in Appendix S2.

4. Analytical results

4.1. Bulk rock composition

The selected samples are characterized by low SiO_2 (40.2–45.2 wt%) and high Al_2O_3 (26.7–27.6 wt%) and MgO (8.15–8.36 wt%) contents (Table S1). Total Fe_2O_3 contents are 19.75 wt% for NLU87 and 11.40 wt% for NLU89. In addition, sample NLU89 contains higher concentrations of CaO, Na_2O, and K_2O than NLU87 (Table S1). Chondrite-normalized REE patterns of the two samples display a similar negative slope from La to Sm and a relatively flat pattern from Gd to Lu (Fig. S3). Sample NLU87 exhibits significantly higher HREE contents and a steeper negative Eu anomaly compared to sample NLU89 (Fig. S3; Table S1).

4.2. Petrography and garnet major element chemistry

Both samples (NLU87 and NLU89) are protomylonitic granulite-facies metapelites, characterized by coarse-grained porphyroclasts embedded in a fine-grained mylonitic matrix, as observed in hand specimens (Fig. 2c, d).

Sample NLU87 is a garnet-rich granulite with coarse-grained garnet porphyroclasts (up to 5 mm in diameter) enclosed within a fine-grained, foliated assemblage of kyanite, quartz, garnet, rutile, and gedrite (Fig. 2c and S1a). X-ray maps of the major element composition, chemical profiles, and inclusion assemblages reveal that these garnet porphyroclasts exhibit three distinct compositional domains referred to as G1, G2, and G3 (Fig. 3a-e). G1 contains numerous mineral inclusions of plagioclase, quartz, biotite, and ilmenite. This garnet displays a fairly flat X_{Alm} (0.63–0.65), X_{Py} (0.31–0.32), X_{Sps} (~0.02), and X_{Grs} (0.02–0.03) composition profile. Garnet G2, which constitutes the largest portion of the phase (~47 vol.%), is relatively inclusion-poor (Figs. 3a,b,c and S1). Inclusions of sillimanite, quartz, spinel, and biotite are observed in this part of the garnet (Fig. 3a,e). Individual inclusions of plagioclase, cordierite, and ilmenite are also present in garnet G2. G2 displays Fe–Mg exchange zoning characterized by outward-decreasing almandine and increasing pyrope contents, X_{Alm} = 0.53–0.64, X_{Py} = 0.31–0.42, $X_{Sps} \approx$ = 0.02, and $X_{Grs} \approx$ 0.04. Toward G3, X_{Py} increases to its maximum value (0.49), whereas X_{Alm}, X_{Sps}, and X_{Grs} decrease to their minimum values (0.49, 0.01, and 0.01, respectively; Fig.3c,d). G3 marks the transition from the inclusion-poor domain to the inclusion-rich margin, where kyanite, quartz, and rutile occur as inclusions (Fig. 3b). In some cases, garnet porphyroclasts are partly replaced by biotite, quartz, and possible cordierite (Fig. 3f). Subhedral poikiloblastic garnet in the mylonitic matrix contains an inclusion assemblage similar to that of G3 (Fig. 3g). The fine-grained matrix aggregates are interpreted as pseudomorphs after cordierite, similar to those reported by Nguyen et al. (2023). Relict cordierite can still be observed within these aggregates (Fig. 3h). Spinel occurs as interstitial grains between garnet porphyroclasts and is partly replaced by kyanite (Fig. 3i).

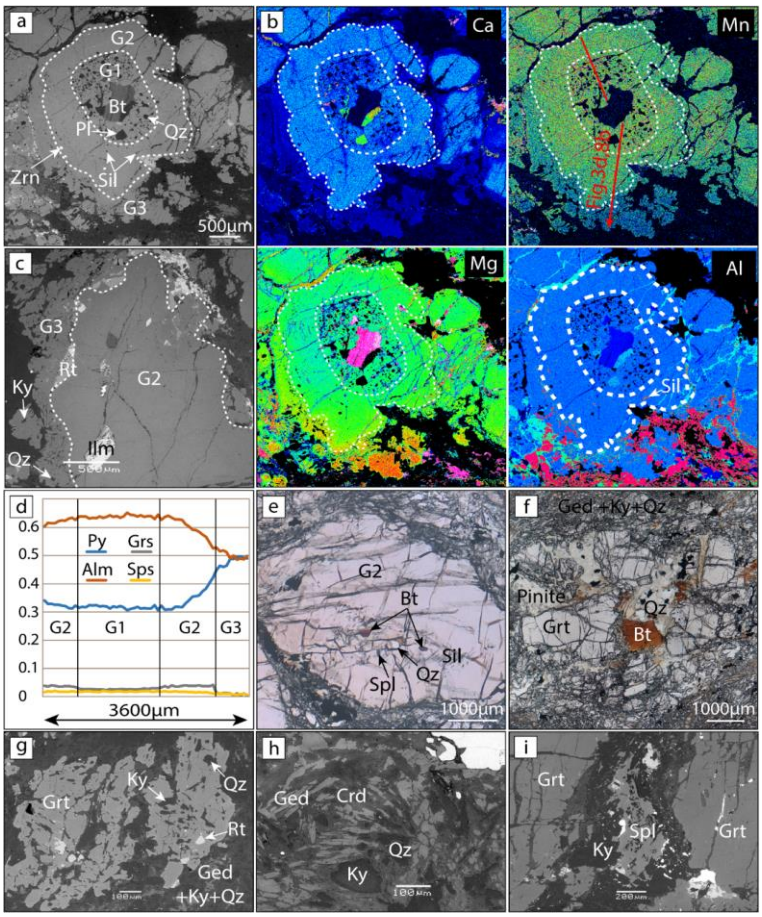

Figure 3. Microstructures, X-ray elemental maps, and chemical profiles of garnet in sample NLU87. (a) BSE image of a garnet porphyroclast with the core containing numerous inclusions of plagioclase, biotite, and quartz. (b) Ca–Mn–Mg–Al elemental zoning of the garnet grain is shown in Fig. 3a. (c) BSE image of a garnet porphyroclast showing the transition from an inclusion-poor mantle to an inclusion-rich rim. (d) Zoning profiles for garnet. (e) Garnet quartz contains inclusions of spinel, quartz, biotite, and sillimanite. (f) Garnet is partly replaced by biotite, quartz, and possible cordierite (pinite). (g) A poikiloblastic garnet in mylonitic fabric is rich in inclusions of kyanite, quartz, and rutile. (h) Cordierite breaks down into gedrite, kyanite, and quartz. (i) Spinel partly replaced by kyanite

Sample NLU89 shows a similar mineral assemblage, except that it contains much more feldspar (both plagioclase and K-feldspar) and biotite (Figs. 2d and 4a), and cordierite breaks down into an orthopyroxene-bearing assemblage instead of a gedrite-bearing assemblage as observed in sample NLU87 (Fig. 4b, c). The coarse-grained porphyroclasts include garnet, plagioclase, and K-feldspar, whereas the fine-grained matrix comprises kyanite, quartz, garnet, orthopyroxene, biotite, and rutile (Figs. 2d and 4a-d). Unlike the coarse-grained garnet in NLU87, the garnet (up to 1 cm in diameter) in this sample exhibits only two compositional domains that contain inclusion assemblages similar to those observed in the G2 and G3 compositional domains of sample NLU87. Based on this petrographic similarity, these two domains in NLU89 are referred to as G2 and G3, respectively. G2 contains inclusions of sillimanite, spinel, corundum, quartz,

K-feldspar, plagioclase, and biotite, with quartz often mantled by a thin film of K-feldspar and biotite mantled by spinel and corundum (Fig. 4d-f). The chemical profiles and elemental maps of the garnet G2 show little major element zoning, with a slight increase in X_{Alm} (0.58 to 0.60), a slight outward decrease in X_{Py} (0.35 to 0.33), whereas X_{Grs} (0.03–0.04) and X_{Sps} (0.02–0.03) remain relatively constant (Fig. 4d, g). Toward G3, a sharp increase is observed in the X_{Py} content, reaching its maximum value (0.49), whereas the X_{Alm} and X_{Sps} contents decrease to their minimum values (0.46 and 0.01, respectively; Fig. 4g). In contrast, X_{Grs} in G3 are variable, ranging from 0.02 to 0.05 (Fig. 4g). G3 and the fine-grained garnet in the mylonitic matrix are rich in orthopyroxene, kyanite, and quartz inclusions (Fig. 4c). In addition to being present as inclusions in garnet G2, corundum and spinel also occur in the matrix, where these are being replaced by kyanite (Fig. 4h). Coarse-grained plagioclase (high-Ca) is partly replaced by a fine-grained assemblage of plagioclase (low -Ca), kyanite, and quartz (Fig. 4i).

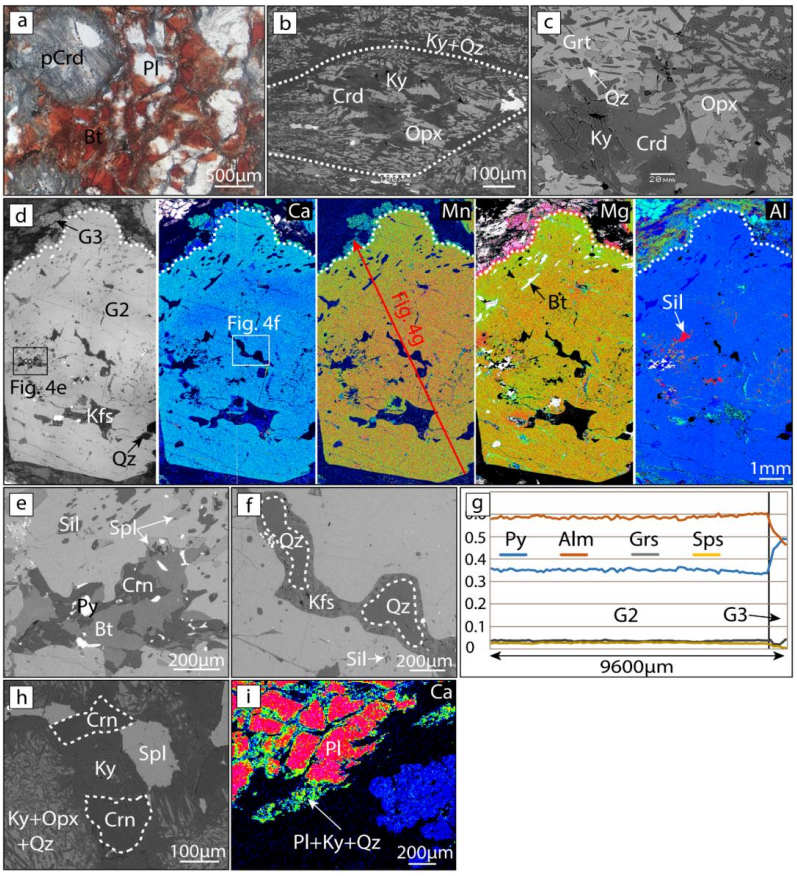

Figure 4. Microstructures, X-ray elemental maps, and chemical profiles of garnet in sample NLU89. (a) Plagioclase- and biotite-rich domain. (b) Cordierite breaks down into orthopyroxene, kyanite, and quartz. (c) Cordierite is replaced by garnet, orthopyroxene, and kyanite. (d) BSE image and Ca–Mn–Mg–Al elemental zoning in garnet. (e) Biotite inclusion in the garnet G2 is being replaced by corundum and spinel. (f) Thin K-feldspar film around quartz in garnet G2. (g) Zoning profiles for garnet. (h) Spinel and corundum are replaced by kyanite. (i) High-Ca plagioclase partially replaced by low-Ca plagioclase + kyanite + quartz. pCrd = Pseudomorph Crd

The accessory phases in the granulite samples included monazite, apatite, zircon, and xenotime. Monazite occurs in various textural settings, including: (1) as inclusions in garnet G1 associated with quartz-plagioclase-biotite-ilmenite assemblages (Fig. 5a); (2) in garnet G2 associated with sillimanite-spinel-corundum-biotite assemblages (Fig. 5b) or as individual grains (Fig. 5c); (3) within fractures of garnet porphyroclasts (Fig. 5d); (4) associated with G3 and subhedral poikiloblastic garnets in the matrix (Fig. 5e, f); and (5) associated with fine-grained, kyanite-bearing matrix assemblages (Fig. 5g). zircon occurs in textural settings similar to those of monazite (Figs. 3a and 5g, h), whereas apatite is restricted to garnet G1 (Fig. 5a). xenotime is only present as tiny inclusions in monazite that is hosted by garnet G1 (Fig. 6a).

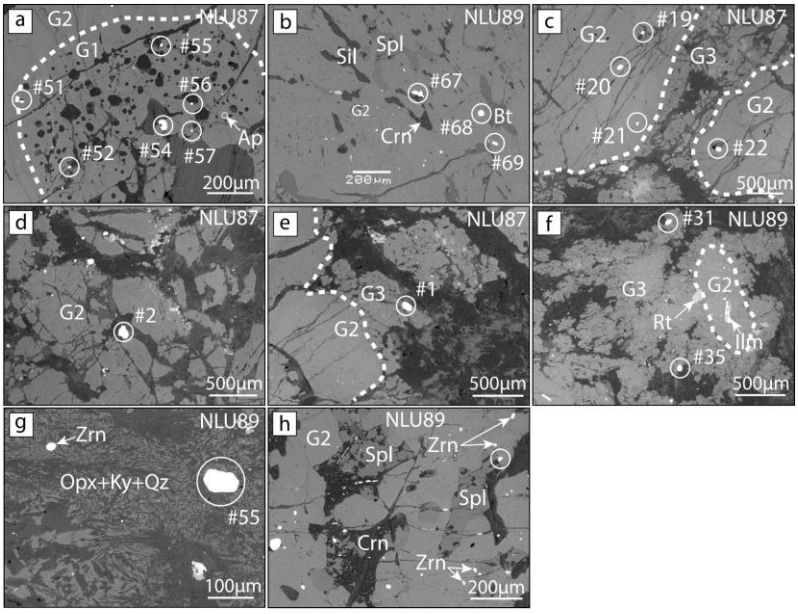

Figure 5. Monazite grains in different textural settings. (a) Monazite inclusions in the garnet G1. (b) Monazite inclusions in the garnet G2. (c) Individual monazite grains are included in the garnet G2. (d) Monazite within the fracture of garnet G2. (e-f) Monazite associated with the garnet G3. (g) Monazite and zircon in a fine-grained assemblage of orthopyroxene, kyanite, and quartz. (h) Zircons in garnet G2. White circles represent monazite localities

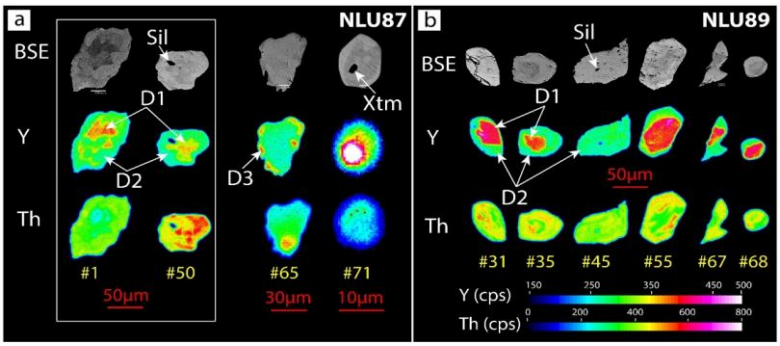

Figure 6. BSE images and Y-Th compositional maps of representative monazite grains from samples NLU87 (a) and NLU89 (b). Color bars are applied to both figures, with units in cps (counts per second)

4.3. Trace element chemistry and U–Pb monazite geochronology

4.3.1. Monazite

Based on the compositional variations, textural settings, and ages of the monazite grains from the two samples, three distinct monazite domains were identified (D1, D2, and D3; Figs. 6 and 7). Domain D1 corresponds to monazite cores, defined by high Y contents (mean = 8463 ppm in sample NLU87 and 14145 ppm in sample NLU89), elevated HREE contents, and relatively low Th (mean = 51032 ppm in sample NLU87 and 49426 ppm in sample NLU89) (e.g., grains 1 and 40, Fig. S2a; grains 7, 8, and 9, Fig. S2b; Table S3). Domain D2 is characterized by low Y (mean = 1598 ppm in sample NLU87 and 4000 ppm in sample NLU89), depleted HREE, and high Th (mean = 58875 ppm in sample NLU87 and 50085 ppm in sample NLU89), overgrows the D1 cores (Figs. 6 and S2a; Table S3). Domain D3 is defined as the outermost rim, with high Y (mean = 7504 ppm) and intermediate HREE, forming overgrowths on the existing D2 domain (e.g., grains 2, 34, and 64; Fig. S2a; Table S3).

Monazite grains hosted in garnet G1 from sample NLU87 exhibit sub-rounded to rounded morphologies, with grain sizes ranging from 10 to 30 μm (e.g., grains 51–60 and 66–71, Figs. 5a and S2a). These grains generally exhibit high Y contents and low Th concentrations. Owing to their small size, trace element analyses could not be conducted. A single U–Pb analysis yields a $^{206}Pb/^{238}U$ date of 433 ± 6 Ma (grain 54; Fig. S2a; Table S2). Other monazite grains range in size from ~20 to 200 μm, and the three compositional domains (D1–D3) are collectively observed among these grains (Figs. 5c-e, S1a, S2a, and 6a). The D1 domain, appearing as patchy or embayed cores, is characterized by high Y + HREE contents, Th/U ratios of 31 to 140, and moderate negative Eu anomalies (mean Eu/Eu^{*} = 0.35; Figs. 6a and 7a; Table S3). Ten U–Pb analyses of ten D1 domains yield $^{206}Pb/^{238}U$ dates ranging from 439 to 410 Ma, with a weighted mean age of 425.9 ± 3.3 Ma (MSWD = 2.7, n = 10, Fig. 7c; Table S2). Probability density and histogram plots of this domain show a single dominant age population, with no clear evidence for bimodality (Fig. S4). In contrast, the D2 domain is depleted in Y + HREE and enriched in Th, with a more pronounced negative Eu anomaly (mean Eu/Eu* = 0.15, Fig. 7a; Table S3) and a wider range of Th/U ratios (45–1023). A total of 20 U–Pb analyses were conducted on 18 grains, yielding dates between 433 and 408 Ma, of which two analyses are discordant. The remaining data define a weighted mean age of 420.3 ± 2.7 Ma (MSWD = 2, n = 18, Fig. 7c; Table S2). Domain D3 is only observed in this sample and is restricted to grains within garnet fractures (e.g., grains 2, 34, 64, and 65; Fig. S1a). Compared to D2, this domain is enriched in Y + HREE. Although the dates obtained from D3 monazite are largely discordant, two concordant analyses yield dates of approximately 390 Ma.

Monazite grains in sample NLU89 are present across all textural settings, with grain sizes ranging from approximately 10 to 100 μm and exhibiting prismatic, rounded, and sub- to euhedral morphologies (Figs. 6b, S1b, and S2b). Most grains show growth zoning with sharp, well-defined boundaries in the core-rim relationships (Fig. 6b). Two compositional domains, D1 and D2, are preserved in the monazites (Fig. 6b). The D1 cores are enriched in Y + HREE, display moderate negative Eu anomalies (mean Eu/Eu* = 0.30), and have Th/U ratios ranging from 49 to 72 (Fig. 7b; Table S3). U–Pb analyses of the D1 monazite domains yield $^{206}Pb/^{238}U$ dates between 426 and 446 Ma, with a weighted mean age of 435.2 ± 2.4 Ma (MSWD = 1.3; n = 18,

Fig. 7d; Table S2). Conversely, the D2 domains are depleted in Y + HREE, have Th/U ratios of 55–75, and display stronger negative Eu anomalies (mean = Eu/Eu* 0.15, Fig. 7b; Table S3). Compared to sample NLU87, the boundary between D1 and D2 is sharper. A total of 21 U–Pb analyses on 18 grains yield $^{206}Pb/^{238}U$ dates from 428 to 403 Ma, with two discordant analyses. The concordant analyses yield a weighted mean age of 422 ± 2.2 Ma (MSWD = 0.56, n = 19, Fig. 7d; Table S2).

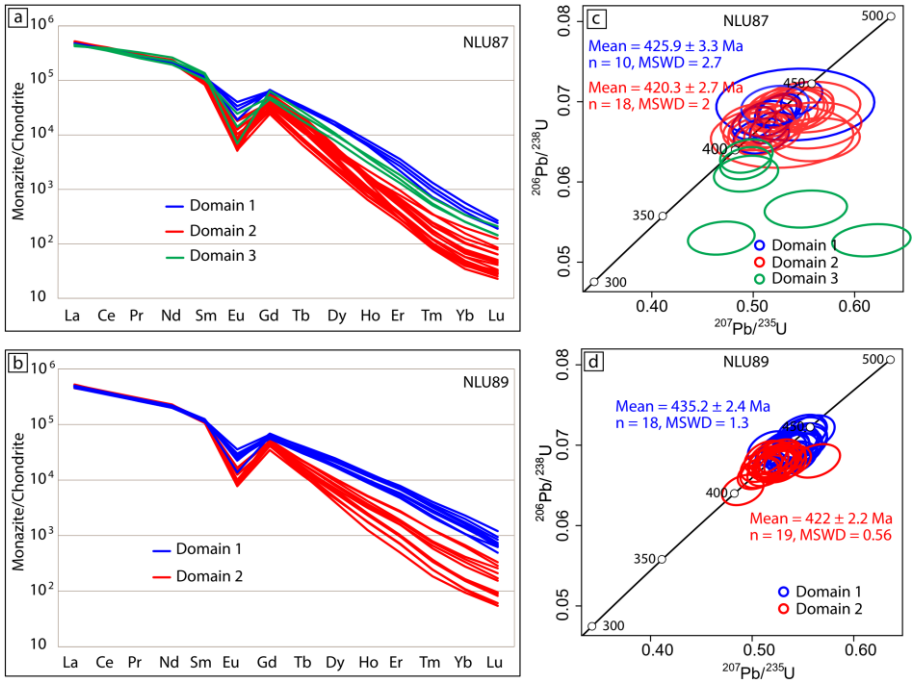

Figure 7. Chondrite-normalized REE spider diagrams and U–Pb concordia diagrams for monazite. (a-b) Sample NLU87. (c-d) Sample NLU89. The uncertainties of mean ages are given at the 2σ level.

4.3.2. Garnet

Based on petrographic features, REE concentrations were analyzed in all garnet domains of both samples. The chondrite-normalized REE patterns and Y + REE profiles of these garnet domains from sample NLU87 show distinct compositional zoning consistent with Ca zoning (Figs. 3b and 8a, b). Garnet G1 exhibits the highest concentrations of Y (mean = 824 ppm) and HREEs, with moderately abundant MREE (except for Tb), a weakly positive HREE pattern, and noticeable negative Eu anomalies (mean Eu/Eu* = 0.27; Table S3). The G2 domain displays lower Y (mean = 209 ppm) and HREE abundances, a flat HREE pattern, and is slightly enriched in Sm, accompanied by stronger negative Eu anomalies (mean Eu/Eu* = 0.17, Table S3). From G2 to G3, a sharp decrease is observed in the relative abundances of Y (mean = 4 ppm), MREE, and HREE, which result in a steep negative slope of the HREEs (Fig. 8a, b). LREE concentrations are close to the detection limit and are indistinguishable across the garnet zoning (Fig. 8a; Table S3). The G3 domain is also characterized by variable Eu anomalies, ranging from small negative to small positive (Eu/Eu^* = 0.26–2.00, Table S3).

REE analyses of a large garnet grain from sample NLU89 show a well-developed compositional zoning pattern (Fig. 8c,d). The Y and HREE concentrations in the garnet G2 gradually decrease outward within this domain,

with Y decreasing from 580 to 163 ppm, consistent with Rayleigh-type fractionation during garnet growth (Fig. 8c, d, and Fig. S1b; Table S3). In contrast, the MREEs remain relatively uniform, with minor variations, including a slight decrease in Dy and an increase in Sm (Fig. 8d; Table S3). The light rare earth elements (LREE) show an overall decreasing trend outward (Table S3). G2 exhibits pronounced negative Eu anomalies with a mean Eu/Eu^* of 0.15 (Fig. 8c; Table S3). Toward the rim (G3), the relative abundance of LREE increases, whereas Y (mean = 3 ppm) and the MREE–HREE contents decrease sharply, reflected in the negative slope of the HREE (Fig. 8c, d). Their Eu anomalies range from weakly negative to weakly positive (Eu/Eu^* = 0.31–2.04; Table S3).

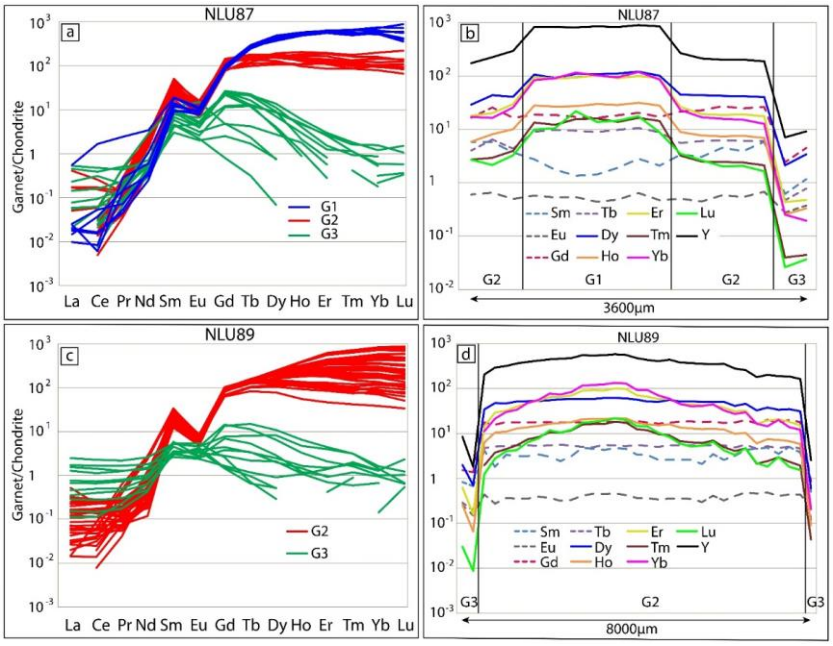

Figure 8. Chondrite-normalized REE diagrams and REE profiles of garnet. (a-b) NLU87. (c-d) NLU89

5. Discussions

5.1. Metamorphic mineral assemblages

Petrographic observations and the chemical characteristics of garnet from both samples suggest the presence of three distinct domains (G1–G3). Each sample contains a different combination of these domains, each hosting a distinct inclusion assemblage. Garnet G1 is observed only in NLU87 and contains inclusions of plagioclase, quartz, biotite, and ilmenite (Fig. 3a). These inclusions, along with garnet G1, are interpreted to have formed during the prograde metamorphic stage. Garnet G2, found in both samples, contains a similar inclusion assemblage, including cordierite + sillimanite + spinel + quartz + biotite + plagioclase + ilmenite ± K-feldspar ± corundum (Figs. 3e and 4d–f). These inclusion phases can also be observed as relics being replaced by fine-grained mineral phases in the matrix (Figs. 3h, i, and 4b, c, h). Thus, the assemblage garnet G2 + sillimanite + spinel + quartz + biotite + plagioclase + ilmenite ± K-feldspar ± corundum + cordierite is considered to represent the peak metamorphic mineral assemblage. The breakdown of biotite into spinel, corundum, and sillimanite, and the presence of thin films of K-feldspar, indicate that melt was present during this stage of metamorphism (Fig. 4e, f;

Vernon, 2011). The development of biotite and quartz at the expense of garnet porphyroclasts likely records retrograde metamorphism (Fig. 3f), similar to that reported by Nguyen et al. (2023). Subhedral poikiloblastic garnet in the matrix and garnet G3 are observed in both samples. They are interpreted to have formed during a later overprinting metamorphic event, coeval with the formation of fine-grained kyanite, quartz, orthopyroxene/gedrite, rutile, and biotite. The metamorphic mineral assemblages are summarized in Table S4.

5.2. Linking monazite domains to garnet formation

Textural relationships and trace element patterns are useful for linking monazite formation to the growth of other major and accessory minerals, such as garnet, thereby adding absolute time to the rock *P–T* path (Buick et al., 2010; Dumond et al., 2015; Mottram et al., 2014; Petrík et al., 2019). No systematic age difference was observed between the analyzed monazite grains included in garnet and those in the matrix, or this may be due to the limited precision of the laser ablation in situ methodology in resolving distinct age populations. Investigating whether a monazite domain crystallized in chemical equilibrium with a specific garnet portion is primarily done by comparing the concentrations of trace elements between these phases (Benetti et al., 2024; Hermann and Rubatto, 2003; Sorger et al., 2024; Warren et al., 2019).

The domain D1 monazite is richer in Y+HREE and relatively depleted in Th compared to domain D2, suggesting that garnet was either absent or less abundant during monazite D1 crystallization (Benetti et al., 2024; D'Souza et al., 2021; Hermann and Rubatto, 2003; Rubatto et al., 2006). This interpretation is supported by petrographic observations showing that garnet G1 is absent in one sample and occurs at low modal abundance in the other (Fig. S1a, b). Additionally, xenotime occurs as tiny inclusions within high-Y, low-Th monazite (D1) enclosed in garnet G1 (Fig. 6a) and is absent elsewhere in the rock, indicating that xenotime crystallized before or during the earliest stages of monazite growth. The enrichment of Y+HREE in both monazite D1 and garnet G1 likely resulted from xenotime breakdown during their initial growth stages (Pyle et al., 2001; Spear and Pyle, 2010). Together, these observations indicate that monazite D1 crystallized contemporaneously with garnet G1.

Conversely, D2 monazite is depleted in Y+HREE, indicating that this domain formed during or after substantial garnet growth, as garnet strongly partitions these elements (Kohn et al., 2005; Regis et al., 2016). This is consistent with the abundance of garnet G2 in both samples (Fig. S1a, b). Depleted-Y monazite (D2) is ubiquitously present as inclusions in garnet G2, indicating the coeval formation of these mineral pairs (Pyle et al., 2001). In addition, both garnet G2 and monazite D2 contain inclusions of sillimanite (Figs. 3e, 4d, e, and 6a, b). Furthermore, a general trend of stronger negative Eu anomalies is observed from monazite D1 to D2 and garnet G1 to G2, consistent with K-feldspar growth as a result of biotite breakdown (Fig. 4e; Bhowmik et al., 2014; Dumond et al., 2015). The coeval crystallization of garnet and monazite typically exhibits Eu anomalies of similar magnitudes and signs (Buick et al., 2010; Hermann and Rubatto, 2003; Kelly et al., 2006; Rubatto et al., 2006). The outward decrease in Y and HREE concentrations within garnet G2 in sample NLU89 is interpreted to reflect Rayleigh-type fractionation during garnet growth in the presence of melt (Otamendi et al., 2002). These observations confirm the chemical equilibrium between garnet G2 and monazite D2 during anatectic melting. It should be

noted that zircon has a similar occurrence to monazite in the studied samples, and zircon is predicted to grow under suprasolidus conditions (Yakymchuk, 2023), suggesting that zircon and monazite may have formed coevally in the presence of melt. Such coeval zircon growth can further contribute to HREE depletion in monazite (Tual et al., 2022), implying that the overall HREE drop likely reflects the combined effects of garnet and zircon growth.

The outermost rims of the monazite grains (D3) are observed exclusively in sample NLU87 and along fractures within coarse-grained garnet (G2) (Fig. 5d), implying that their formation postdated G2 garnet growth. The enrichment of Y+HREE in D3 monazite suggests that garnet decomposition was responsible for this chemical signature. Garnet breakdown contributes significant amounts of Y+HREE to newly formed monazite rims (Dumond et al., 2015; Kohn et al., 2005; Sorger et al., 2024). An alternative interpretation involving the breakdown of other HREE-competing phases, such as allanite or xenotime, is unlikely, given the virtual absence of these phases in the rock matrix.

Garnet G3 and fine-grained garnet in the mylonitic fabric show marked differences in both major and trace elements compared to garnet G1 and G2 (Figs. 3b, d, 4d, g, and 8a-d). These differences indicate a distinct episode of garnet growth, rather than continuous growth with the formation of garnet G1 and G2. This is consistent with a previous study suggesting that fine-grained garnet formed under subsolidus amphibolite-facies conditions (600°C and 7.3 kbar) and was favored by a later mylonitization event (Nguyen et al., 2023). Garnet G3 is interpreted to have achieved local chemical equilibrium within the mylonitic domains (Nguyen et al., 2023; this study). Because earlier garnet growth (G1 and G2) had already sequestered a large proportion of heavy rare earth elements (HREEs), the effective HREE budget available during the formation of G3 was limited. As a result, garnet G3 is characterized by lower HREE concentrations, reflecting growth from an HREE-depleted reservoir. Considering that high-strain zones frequently undergo fluid influx (Stenvall et al., 2020), monazite may be subject to fluid-mediated dissolution-reprecipitation at low temperatures (Harlov et al., 2011; Taylor et al., 2016). The breakdown of cordierite into garnet + orthopyroxene + kyanite + quartz in sample NLU89 (Fig. 4c) indicates that the second metamorphic event occurred under fluid-absent conditions. In addition, the formation of gedrite in sample NLU87 does not necessarily require the addition of external fluids, because cordierite in granulite-facies rocks commonly contains up to ~2 wt% H_2O (Harley and Carrington, 2001). The breakdown of such hydrous cordierite typically produces orthoamphibole-bearing assemblages (Diener et al., 2008). All these lines of evidence suggest that monazite did not grow or become affected during the formation of garnet G3, even though several grains appear to be in textural equilibrium with garnet G3 (Fig. 5e, f). An increase in LREE and weakly negative to weakly positive Eu anomalies in garnet G3 (Fig. 8c) could reflect the breakdown of feldspars (Fig. 4i; Hermann and Rubatto, 2003).

5.3. Metamorphic P-T-t path

Monazite dates range from approximately 440 to 390 Ma, suggesting a single Early Paleozoic high-temperature metamorphic cycle that overlaps with zircon ages of ~440–410 Ma (Bui et al., 2022; Nguyen et al., 2023). Zircon from granulite-facies rocks in the study area exhibits a core-rim structure, in which the cores are considered to be inherited detrital grains, whereas the rims are interpreted to record the timing of high-temperature metamorphism (Bui et al., 2022; Nguyen et al., 2023). However, the lack of

distinct metamorphic growth zones and robust petrochronological constraints makes it difficult to directly link zircon ages to specific segments of the metamorphic P–T path (Nguyen et al., 2023).

In contrast, monazite in the studied samples preserves well-defined compositionally zoned domains, and the ages are distinguishable between these domains. For monazite, closure temperatures of ~800–850°C have been inferred based on the preservation of age relationships in high-temperature metamorphic rocks (Spear and Parrish, 1996; Bingen and van Breemen, 1998; Kamber et al., 1998). However, experimental diffusion studies demonstrate that Pb diffusion in monazite is extremely slow under dry conditions, resulting in a high closure temperature exceeding 900°C (Cherniak et al., 2004). Given that the studied samples are melt-depleted granulite facies rocks formed under fluid-poor conditions, monazite therefore has the potential to preserve the timing of prograde and peak metamorphic stages. In addition, monazite is more reactive than zircon (Rubatto et al., 2012). It may recrystallize and undergo compositional modification during retrograde metamorphism due to dissolution-precipitation in the presence of fluids (Harlov et al., 2011). Thus, the ages recorded by monazite domains in the studied samples may reflect distinct metamorphic stages.

High-Y monazite cores (D1) yield weighted mean ages of 425.9 ± 3.3 Ma and 435.2±2.4 Ma for samples NLU87 and NLU89, respectively. These ages may represent the timing of prograde metamorphism corresponding to the growth of garnet G1. However, the patchy/lobate zoning of monazite cores in NLU87 indicates partial resetting of this domain by anatectic melt via biotite breakdown at or near peak conditions (Bhowmik et al., 2014; Dumond et al., 2015). This interpretation is supported by petrographic evidence showing that biotite breakdown generated the peak mineral phases (Fig. 4e). The overlap of the weighted mean ages between monazite D1 and D2 (Fig. 7c) in this sample can be attributed to the partial- to complete-resetting of monazite ages. Conversely, monazite D1 in sample NLU89 exhibits sharp grain boundaries (Figs. 6b and S2b) and yielded a weighted mean age of 435.2 ± 2.4 Ma (Fig. 7d). This age constrains the timing of monazite D1 crystallization during prograde metamorphism.

Monazite ages in granulite facies rocks are commonly interpreted to record cooling and crystallization from anatectic melts (Benetti et al., 2024; Taylor et al., 2016; Weller et al., 2020). Monazite D2 in the studied samples is interpreted to have grown during garnet G2 formation. If monazite D2 crystallized from the melt, the majority of garnet would have grown during melt crystallization because this monazite D2 occurs as inclusions throughout the garnet G2. However, the studied rocks (Table S1) are highly depleted in SiO_2 and enriched in MgO, FeO, and Al_2O_3, suggesting that a significant quantity of melt was lost during anatexis (Stepanov et al., 2024). Minimal quantities of melt may have been retained in the system. Therefore, garnet G2 is considered a peritectic phase. In addition, monazite crystallized from anatectic melts typically shows elevated Y concentrations, which are not observed in this domain (Barnes et al., 2021; Corrie and Kohn, 2011; Kohn et al., 2005). Furthermore, the increase in Th from D1 to D2 monazite is consistent with increasing metamorphic grade (Yakymchuk and Brown, 2019). Collectively, the consistent weighted mean age of ~420 Ma (Fig. 7c, d) obtained from monazite D2 in both samples is interpreted to represent the timing at or near the peak conditions.

Monazite D3 yielded younger dates down to approximately 390 Ma (Fig. 7c). The highly discordant U–Pb ages of this monazite domain suggest disturbance of isotopic systematics by coupled dissolution-reprecipitation (Harlov et al., 2011). As noted above, monazite D3 occurs within fractures of

coarse-grained garnet (G2), and the dates obtained from this domain are therefore interpreted to reflect the timing of retrograde metamorphism under subsolidus conditions.

Petrographic examination and mineral chemical characteristics indicate that the Dai Loc Early Paleozoic rocks were overprinted by a later metamorphic cycle (Nguyen et al., 2023). This later metamorphic cycle has been linked to the development of NW-SE-trending shear zones in the eastern Indochina Block during the Triassic collision between the Indochina and South China blocks (Faure et al., 2018; Lepvrier et al., 1997). However, U–Pb geochronology studies of both monazite and zircon show no imprint of this tectonothermal event. This absence is interpreted to reflect metamorphic conditions that were insufficient to induce either Pb diffusion or fluid-assisted dissolution-reprecipitation in these accessory phases (Cherniak and Watson, 2000; Williams et al., 2011). A likely explanation is the low-temperature metamorphic peak (600°C) and the absence of fluid during the second cycle.

In summary, combined with U–Pb zircon ages from both metamorphic rocks and syn-metamorphic intrusions, the Dai Loc granulite-facies rocks are interpreted to record prograde metamorphism at 440–430 Ma, peak conditions at 430–420 Ma, and melt crystallization probably between 420 and 390 Ma. A schematic P–T–t diagram showing the relationships between Mnz growth and Grt formation is presented in Fig. 9.

Although the *P–T* conditions for Early Paleozoic granulite-facies rocks in the KTM are poorly constrained, petrological studies suggest low-pressure high-temperature metamorphism, with the timing constrained to 450–430 Ma (Nakano et al., 2013; Roger, 2007; Bui et al., 2020). Previous studies indicate that high-grade metamorphic rocks in the Dai Loc shear zone were also metamorphosed under low-pressure high-temperature conditions (Nguyen et al., 2023). These similarities suggest that Early Paleozoic metamorphism in both the TBS and KTM may have developed within a similar tectonic setting. Recent studies propose that subduction followed by collision between the TSB and KTM along the TK-PS suture zone occurred during the Early Paleozoic (Gardner et al., 2017; Jiang et al., 2020; Ngo et al., 2022, 2025a; Tran et al., 2020; Wang et al., 2021). This is indicated by the occurrence of arc-related magmatism in both regions during ~520–460 Ma (Tran et al., 2020; Nguyen et al., 2021; Ngo et al., 2025a; Wang et al., 2020; Wang et al., 2021), while high-pressure metamorphism suggests the collision had taken place before ~450 Ma (Usuki et al., 2009). Furthermore, Wang et al. (2021) proposed that ~440 Ma in the KTM marks a transition from syn- to post-collisional tectonics, consistent with widespread late Ordovician-Silurian post-collisional magmatism in the region (Ngo et al., 2025a, 2025 b; Jiang et al., 2020). The Early Paleozoic rocks in the Dai Loc shear zone have also been interpreted to form in a post-collisional extensional tectonic setting (Nguyen et al., 2023). Collectively, these observations between the TBS and KTM indicate a regional Early Paleozoic tectonic phase that affected the entire eastern Indochina Block.

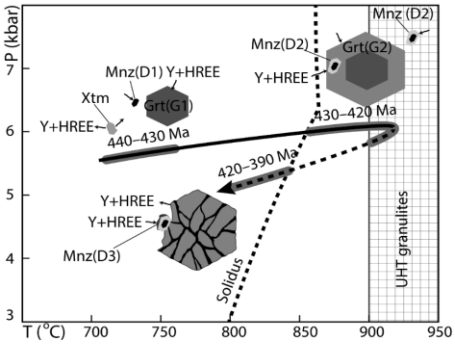

Figure 9. Early Paleozoic *P–T-t* path for the Dai Loc granulites. The P–T path inferred by Nguyen et al. (2023): the bold line indicates the well-constrained prograde-to-peak P–T path, and the dashed line represents a schematic retrograde cooling path. The solidus is shown schematically, as in Nguyen et al. (2023)

6. Conclusions

The metamorphic evolution of the Dai Loc shear zone is characterized by a well-defined sequence of prograde, peak, and retrograde stages during the Early Paleozoic. The integration of in-situ monazite geochronology, trace element geochemistry, and petrography revealed that monazite preserves three distinct growth domains. These domains are closely linked to garnet growth and breakdown, recording a monazite growth episode during prograde metamorphism at ~435 Ma, peak metamorphic conditions at ~420 Ma, and retrograde metamorphism at ~390 Ma, respectively. The U–Pb data provide robust evidence for a high-grade metamorphic history between 440 and 390 Ma, consistent with regional zircon U–Pb data, and contribute to a broader understanding of Early Paleozoic tectonometamorphism in the Indochina block. These findings indicate that a comprehensive analysis of chemical and petrographic data is essential for accurately reconstructing the crystallization and dissolution history of geochronometers. The identification of chemical signatures from accessory phase-forming reactions in major phases, such as garnet, can aid in reconstructing complex metamorphic evolution by linking ages to specific metamorphic stages.

Acknowledgements

This study was financially supported by grants from the National Science and Technology Council, Taiwan, ROC (109-2116-M-002-013 and 110-2116-M-002-029). We thank Yu-Shiang Wang for his assistance with BSE imaging, and Dr. Hao-Yang Lee and Emily for their help with LA–ICP–MS analyses.

Reference

Barnes C.J., Majka J., Jeanneret P., Ziemniak G., Kooijman E., Kosminska K., Kielman-Schmitt M., Schneider D.A., 2021. Using Th–U–Pb geochronology to extract crystallization ages of Paleozoic metamorphic monazite contaminated by initial Pb. Chem. Geol., 582, 120450. https://doi.org/10.1016/j.chemgeo.2021.120450.

Benetti B., Neto M.d.C.C., Carosi R., Iaccarino S., Luvizotto G.L., Montomoli C., Langone A., 2024. Continental subduction and exhumation of the lower crust in a hot orogen: Insights from high-pressure (ultra) high-temperature granulite in the Pouso Alto Nappe, Southeast Brazil. Lithos, 482, 107720. https://doi.org/10.1016/j.lithos.2024.107720.

Bhowmik S.K., Wilde S.A., Bhandari A., Sarbadhikari A.B., 2014. Zoned Monazite and Zircon as Monitors for the Thermal History of Granulite Terranes: an Example from the Central Indian Tectonic Zone. J. Petrol., 55(3), 585–621. https://doi.org/10.1093/petrology/egt078.

Bingen B., Van Breemen O., 1998. U-Pb monazite ages in amphibolite-to granulite-facies orthogneiss reflect hydrous mineral breakdown reactions: Sveconorwegian Province of SW Norway. Contrib. Mineral. Petrol., 132, 336–353. https://doi.org/10.1007/s004100050428.

Blereau E., Clark C., Taylor R.J.M., Johnson T.E., Fitzsimons I.C.W., Santosh M., 2016. Constraints on the timing and conditions of high-grade metamorphism, charnockite formation and fluid-rock interaction in the Trivandrum Block, southern India. J. Metamorph. Geol., 34(6), 527–549. https://doi.org/10.1111/jmg.12192.

Breton N.L., Thompson A.B., 1988. Fluid-absent (dehydration) melting of biotite in metapelites in the early stages of crustal anatexis. Contrib. Mineral. Petrol., 99, 226–237. https://doi.org/10.1007/bf00371463.

Bui T.S.V., Kitano I., Tran T.A., Pham N.C., Hoang L.V., Phuong L.P.T., Quoc C.T., 2025. Metamorphism in the A Vuong Formation, southern Truong Son Belt, Vietnam. Vietnam J. Earth Sci., 47(3), 376–395. https://doi.org/10.15625/2615-9783/23301.

Bui T.S.V., Osanai Y., Nakano N., Adachi T., Kitano I., Owada M., 2020. Timing of high-grade metamorphism in the Kontum Massif, Vietnam:

Constraints from zircon-monazite multi-geochronology and trace elements geochemistry of zircon, monazite and garnet. J. Asian Earth Sci., 187, 104084. https://doi.org/10.1016/j.jseaes.2019.104084.

Bui T.S.V., Osanai Y., Nakano N., Adachi T., Kitano I., Owada M., 2022. Petrology and zircon U–Pb geochronology of pelitic gneisses and granitoids from the Dai Loc Complex, Truong Son Belt, Vietnam: Implication for the Silurian magmatic-metamorphic event. J. Asian Earth Sci., 226, 105070. https://doi.org/10.1016/j.jseaes.2021.105070.

Buick I.S., Clark C., Rubatto D., Hermann J., Pandit M., Hand M., 2010. Constraints on the Proterozoic evolution of the Aravalli-Delhi Orogenic belt (NW India) from monazite geochronology and mineral trace element geochemistry. Lithos, 120(3–4), 511–528. https://doi.org/10.1016/j.lithos.2010.09.011.

Burrett C.F., Udchachon M., Thassanapak H., 2021. The Truong Son, Loei-Phetchabun and Kontum Terranes in Indochina: Provenance, Rifting and Collisions. Frontiers in. Front. Earth Sci., 9, 289. https://doi.org/10.3389/feart.2021.603565.

Cat N.H., 1996. Geological Map of Vietnam 1:50000 Scale, Hoi An-Da Nang. South Vietnam Geological Mapping Division, General Department of Geology and Minerals of Vietnam.

Catlos E., Gilley L., Harrison T.M., 2002. Interpretation of monazite ages obtained via in situ analysis. Chem. Geol., 188(3–4), 193–215. https://doi.org/10.1016/s0009-2541(02)00099-2.

Cherniak D.J., Watson E.B., Grove M., Harrison T.M., 2004. Pb diffusion in monazite: A combined RBS/SIMS study. Geochim. Cosmochim. Acta, 68(4), 829–840. https://doi.org/10.1016/j.gca.2003.07.012.

Corrie S.L., Kohn M.J., 2011. Metamorphic history of the central Himalaya, Annapurna region, Nepal, and implications for tectonic models. GSA Bull., 123(9–10), 1863–1879. https://doi.org/10.1130/b30376.1.

D'Souza J., Prabhakar N., Sheth H., Xu Y.G., 2021. Metamorphic P–T–t–d evolution of the Mesoproterozoic Pur-Banera supracrustal belt, Aravalli Craton, northwestern India: Insights from phase equilibria modelling and zircon-monazite geochronology of metapelites. J. Metamorph. Geol., 39(9), 1173–1204. https://doi.org/10.1111/jmg.12606.

Diener J.F.A., White R.W., Powell R., 2008. Granulite facies metamorphism and subsolidus fluid-absent reworking, Strangways Range, Arunta Block, central Australia. J. Metamorph. Geol., 26(6), 603–622. https://doi.org/10.1111/j.1525-1314.2008.00782.x.

Dumond G., Goncalves P., Williams M.L., Jercinovic M.J., 2015. Monazite as a monitor of melting, garnet growth and feldspar recrystallization in continental lower crust. J. Metamorph. Geol., 33(7), 735–762. https://doi.org/10.1111/jmg.12150.

Faure M., Lepvrier C., Nguyen V.V., Vu V.T., Lin W., Chen Z.-C., 2014. The South China Block-Indochina collision: Where, when and how? J. Asian Earth Sci., 79(A), 260–274. https://doi.org/10.1016/j.jseaes.2013.09.022.

Faure M., Nguyen V.V., Hoai L.T.T., Lepvrier C., 2018. Early Paleozoic or Early–Middle Triassic collision between the South China and Indochina Blocks: The controversy resolved? Structural insights from the Kon Tum massif (Central Vietnam). J. Asian Earth Sci., 166, 162–180. https://doi.org/10.1016/j.jseaes.2018.07.015.

Gardner C.J., Graham I.T., Belousova E., Booth G.W., Greig A., 2017. Evidence for Ordovician subduction-related magmatism in the Truong Son terrane, SE Laos: Implications for Gondwana evolution and porphyry Cu exploration potential in SE Asia. Gondwana Res., 44, 139–156. https://doi.org/10.1016/j.gr.2016.11.003.

Godet A., Guilmette C., Labrousse L., Davis D.W., Smit M.A., Cutts J.A., Charette B., 2020. Complete metamorphic cycle and long-lived anatexis in the c. 2.1 Ga Mistinibi Complex, Canada. J. Metamorph. Geol., 38(3), 235–264. https://doi.org/10.1130/abs/2020am-352710.

Harley S., Carrington D., 2001. The distribution of H_2O between cordierite and granitic melt: H2O incorporation in cordierite and its application to high-grade metamorphism and crustal anatexis. Journal of Petrology, 42(9), 1595–1620. https://doi.org/10.1093/petrology/42.9.1595.

Harley S.L., 2016. A matter of time: The importance of the duration of UHT

metamorphism. J. Miner. Petrol. Sci., 111(2), 50–72. https://doi.org/10.2465/jmps.160128.

Harlov D.E., Wirth R., Hetherington C.J., 2011. Fluid-mediated partial alteration in monazite: he role of coupled dissolution-reprecipitation in element redistribution and mass transfer. Contrib. Mineral. Petrol., 162, 329–348. https://doi.org/10.1007/s00410-010-0599-7.

Hermann J., Rubatto D., 2003. Relating zircon and monazite domains to garnet growth zones: age and duration of granulite-facies metamorphism in the Val Malenco lower crust. J. Metamorph. Geol., 21(9), 833–852. https://doi.org/10.1046/j.1525-1314.2003.00484.x.

Jiang W., Yu J.H., Wang X., Griffin W.L., Pham T.H., Nguyen D.L., Wang F., 2020. Early Paleozoic magmatism in northern Kontum Massif, Central Vietnam: Insights into tectonic evolution of the eastern Indochina Block. Lithos, 376–377, 105750. https://doi.org/10.1016/j.lithos.2020.105750.

Jiao S., Evans N.J., Mitchell R.N., Fitzsimons I.C.W., Guo J., 2021. Heavy rare-earth element and Y partitioning between monazite and garnet in aluminous granulites. Contrib. Mineral. Petrol., 176, 50. https://doi.org/10.1007/s00410-021-01808-2.

Kelly N.M., Clarke G.L., Harley S.L., 2006. Monazite behaviour and age significance in poly-metamorphic high-grade terrains: a case study from the western Musgrave Block, central Australia. Lithos, 88(1–4), 100–134. https://doi.org/10.1016/j.lithos.2005.08.007.

Kelsey D.E., Clark C., Hand M., 2008. Thermobarometric modelling of zircon and monazite growth in melt-bearing systems: examples using model metapelitic and metapsammitic granulites. J. Metamorph. Geol., 26(2), 199–212. https://doi.org/10.1111/j.1525-1314.2007.00757.x.

Kelsey D.E., Hand M., 2015. On ultrahigh-temperature crustal metamorphism: Phase equilibria, trace element thermometry, bulk composition, heat sources, timescales and tectonic settings. Geosci. Front., 6(3), 311–356. https://doi.org/10.1016/j.gsf.2014.09.006.

Kohn M.J., Engi M., Lanari P., 2017. Petrochronology: Methods and applications. Rev. Mineral. Geochem., 83, 575. https://doi.org/10.1515/9783110561890-009.

Kohn M.J., Wieland M., Parkinson C., Upreti B., 2005. Five generations of monazite in Langtang gneisses: implications for chronology of the Himalayan metamorphic core. J. Metamorph. Geol., 23(5), 399–406. https://doi.org/10.1111/j.1525-1314.2005.00584.x.

Lan C.Y., Chung S.L., Van Long T., Lo C.-H., Lee T.-Y., Mertzman S.A., Shen J.J.S., 2003. Geochemical and Sr–Nd isotopic constraints from the Kontum massif, central Vietnam, on the crustal evolution of the Indochina lock. Precambrian Res., 122(1–4), 7–27. https://doi.org/10.1016/s0301-9268(02)00205-x.

Lepvrier C., Maluski H., Nguyen V.V., Rogues D., Axente V., Rangin C., 1997. Indosinian NW-trending shear zones within the Truong Son belt (Vietnam) Ar-40-Ar-39 Triassic ages and Cretaceous to Cenozoic overprints. Tectonophysics, 283(1–4), 105–127. https://doi.org/10.1016/s0040-1951(97)00151-0.

Lepvrier C., Maluski H., Vu V.T., Leyreloup A., Phan T.T., Nguyen V.V., 2004. The Early Triassic Indosinian orogeny in Vietnam (Truong Son Belt and Kontum Massif); implications for the geodynamic evolution of Indochina. Tectonophysics, 393(1–4), 87–118. https://doi.org/10.1016/j.tecto.2004.07.030.

Lepvrier C., Nguyen V.V., Maluski H., Phan T.T., Vu V.T., 2008. Indosinian tectonics in Vietnam. C. R. Geosci., 340(2–3), 94–111. https://doi.org/10.1016/j.crte.2007.10.005.

Metcalfe I., 2006. Palaeozoic and Mesozoic tectonic evolution and palaeogeography of East Asian crustal fragments: The Korean Peninsula in context. Gondwana Res., 9(1–2), 24–46. https://doi.org/10.1016/j.gr.2005.04.002.

Metcalfe I., 2013. Gondwana dispersion and Asian accretion: Tectonic and palaeogeographic evolution of eastern Tethys. J. Asian Earth Sci., 66, 1–33. https://doi.org/10.1016/j.jseaes.2012.12.020.

Mottram C.M., Cottle J.M., 2024. An electron backscatter diffraction study of monazite: Linking

the time-deformation path. Chem. Geol., 663, 122238. https://doi.org/10.1016/j.chemgeo.2024.122238.

Mottram C.M., Warren C.J., Regis D., Roberts N.M.W., Harris N.B.W., Argles T.W., Parrish R.R., 2014. Developing an inverted Barrovian sequence; insights from monazite petrochronology. Earth Planet. Sci. Lett., 403, 418–431. https://doi.org/10.1016/j.epsl.2014.07.006.

Nakano N., Osanai Y., Owada M., Hayasaka Y., Tran N.N., 2009. Permo-Triassic Barrovian-type metamorphism in the ultrahigh-temperature Kontum Massif, central Vietnam: Constraints on continental collision tectonics in Southeast Asia. Island Arc, 18(1), 126–143. https://doi.org/10.1111/j.1440-1738.2008.00646.x.

Nakano N., Osanai Y., Owada M., Pham B., Hokada T., Kaiden H., Bui T.S.V., 2021. Evolution of the Indochina Block from its formation to amalgamation with Asia: Constraints from protoliths in the Kontum Massif, Vietnam. Gondwana Res., 90, 47–62. https://doi.org/10.1016/j.gr.2020.11.002.

Nakano N., Osanai Y., Owada M., Tran N.N., Charusiri P., Khamphavong K., 2013. Tectonic evolution of high-grade metamorphic terranes in central Vietnam: Constraints from large-scale monazite geochronology. J. Asian Earth Sci., 73, 520–539. https://doi.org/10.1016/j.jseaes.2013.05.010.

Nakano N., Osanai Y., Owada M., Tran N.N., Toyoshima T., Pham B., Tsunogae T., Kagami H., 2007. Geologic and metamorphic evolution of the basement complexes in the Kontum Massif, central Vietnam. Gondwana Res., 12(4), 438–453. https://doi.org/10.1016/j.gr.2007.01.003.

Nakano N., Osanai Y., Owada M., Tran N.N., Tsunogae T., Toyoshima T., Pham B., 2004. Decompression process of mafic granulite from eclogite to granulite facies under ultrahigh-temperature conditions in the Kontum Massif, central Vietnam. J. Miner. Petrol. Sci., 99(4), 242–256. https://doi.org/10.2465/jmps.99.242.

Nakano N., Osanai Y., Sajeev K., Hayasaka Y., Miyamoto T., Nguyen T.M., Windley B.F., 2010. Triassic eclogite from northern Vietnam: Inferences and geological significance. J. Metamorph. Geol., 28(1), 59–76. https://doi.org/10.1111/j.1525-1314.2009.00853.x.

Ngo X.T., Bui V.H., Tran M.D., Kim Y., Xiaochun L., Tran T.H., Khang Q.L., 2022. Ordovician continental arc magmatism in the Tam Ky-Phuoc Son Suture Zone, Central Indochina Block, Southeast Asia. Geol. J., 58(2), 825–836. https://doi.org/10.1002/gj.4626.

Ngo X.T., Luong Q.K., Bui V.H., Tran T.H., Nguyen Q.H., Dinh T.T., 2025b. Petrogenesis of early Paleozoic S-type granitic mylonite. Vietnam Journal of Earth Sciences, 47(3), 337–354. https://doi.org/10.15625/2615-9783/23115.

Ngo X.T., Nguyen Q.H., Kim Y., Kwon S., Bui V.H., Tran T.H., Samuel V.O., 2025a. Cambrian-Ordovician Arc-Related Magmatism in the Central Southeast Asian Continents and Its Significance on Early Palaeozoic Tectonics of the Indochina Block. Geol. J., 60(3), 776–791. https://doi.org/10.1002/gj.5102.

Nguyen D.N., Lo C.H., Usuki T., Iizuka Y., Binh P., 2023. P–T–t conditions of Early Paleozoic low-P high-T granulite-facies metamorphism in the southern Truong Son Belt, central Vietnam. J. Metamorph. Geol., 41(8), 1081–1117. https://doi.org/10.1111/jmg.12737.

Nguyen M.Q., Feng Q.L., Zi J.W., Zhao T.Y., Tran T.H., Ngo X.T., Tran M.D., Nguyen Q.H., 2019. Cambrian intra-oceanic arc trondhjemite and tonalite in the Tam Ky-Phuoc Son Suture Zone, central Vietnam: Implications Connop, 70, 151–170. https://doi.org/10.1016/j.gr.2019.01.002.

Osanai Y., Nakano N., Owada M., Tran N.N., Toyoshima T., Tsunogae T., Pham B., 2004. Permo-Triassic ultrahigh-temperature metamorphism in the Kontum massif, central Vietnam. J. Miner. Petrol. Sci., 99(4), 225–241. https://doi.org/10.2465/jmps.99.225.

Otamendi J.E., de la Rosa J.D., Patiño Douce A.E., Castro A., 2002. Rayleigh fractionation of heavy rare earths and yttrium during metamorphic garnet growth. Geology, 30(2), 159–162. https://doi.org/10.1130/0091-7613(2002)030%3C0159:rfohre%3E2.0.co;2.

Petrík I., Janák M., Klonowska I., Majka J., Froitzheim N., Yoshida K., Sasinková V., Konečný P., Vaculovič T., 2019. Monazite behaviour during metamorphic evolution of a diamond-bearing gneiss: a case study from the Seve Nappe Complex, Scandinavian Caledonides. J. Petrol., 60(9), 1773–1796. https://doi.org/10.1093/petrology/egz051.

Pham T.H., Nguyen T.D., Nguyen T.B.T., Nuyen T.M., Minh P., 2016. U–Pb ages and Hf isotopic composition of zircon and bulk-rock geochemistry of the Dai Loc granitoid complexin Kontum massif: Implications for early Paleozoic crustal evolution in Central Vietnam. J. Miner. Petrol. Sci., 111(5), 326–336. https://doi.org/10.2465/jmps.151229.

Pyle J.M., Spear F.S., Rudnick R.L., McDonough W.F., 2001. Monazite-xenotime-garnet equilibrium in metapelites and a new monazite-garnet thermometer. J. Petrol., 42(11), 2083–2107. https://doi.org/10.1093/petrology/42.11.2083.

Regis D., Warren C.J., Mottram C.M., Roberts N.M.W., 2016. Using monazite and zircon petrochronology to constrain the P–T–t evolution of the middle crust in the Bhutan Himalaya. J. Metamorph. Geol., 34(6), 617–639. https://doi.org/10.1111/jmg.12196.

Roger F., Maluski H., Leyreloup A., Lepvrier C., Thi P.T., 2007. U–Pb dating of high-temperature metamorphic episodes in the Kon Tum Massif (Vietnam). J. Asian Earth Sci., 30(3–4), 565–572. https://doi.org/10.1016/j.jseaes.2007.01.005.

Rubatto D., Chakraborty S., Dasgupta S., 2012. Timescales of crustal melting in the Higher Himalayan Crystallines inferred from trace element-constrained monazite and zircon chronology. Contrib. Mineral. Petrol., 165, 349–372. https://doi.org/10.1007/s00410-012-0812-y.

Rubatto D., Hermann J., Buick I.S., 2006. Temperature and Bulk Composition Control on the Growth of Monazite and Zircon During Low-pressure Anatexis (Mount Stafford, Central Australia). J. Petrol., 47(10), 1973–1996. https://doi.org/10.1093/petrology/egl033.

Sawyer E.W., 2008. Atlas of migmatites: NRC Research press, vol. 9. https://doi.org/10.1139/9780660197876.

Schorn S., Diener J.F., 2019. Seemingly disparate temperatures recorded in coexisting granulite facies lithologies. J. Metamorph. Geol., 37(8), 1049–1078. https://doi.org/10.1111/jmg.12500.

Shi M.F., Lin F.C., Fan W.Y., Deng Q., Cong F., Tran M.D., Zhu H.P., Wang H., 2015. Zircon U–Pb ages and geochemistry of granitoids in the Truong Son terrane, Vietnam: Tectonic and metallogenit implications. J. Asian Earth Sci., 101, 101–120. https://doi.org/10.1016/j.jseaes.2015.02.001.

Skrzypek E., Bosse V., Kawakami T., Martelat J.-E., Štípská P., 2017. Transient allanite replacement and prograde to retrograde monazite (re)crystallization in medium-grade metasedimentary rocks from the Orlica-Śnieżnik Dome (Czech Republic/Poland): Textural and geochronological arguments. Chem. Geol., 449, 41–57. https://doi.org/10.1016/j.chemgeo.2016.11.033.

Sorger D., Hauzenberger C.A., Finger F., Linner M., Skrzypek E., Schorn S., 2024. Formation of low-pressure reaction textures during near-isothermal exhumation of hot orogenic crust (Bohemian Massif, Austria). J. Metamorph. Geol., 42(1), 3–34. https://doi.org/10.1111/jmg.12744.

Spear F.S., Pyle J.M., 2010. Theoretical modeling of monazite growth in a low-Ca metapelite. Chem. Geol., 273(1–2), 111–119. https://doi.org/10.1016/j.chemgeo.2010.02.016.

Stenvall C., Fagereng A., Diener J., Harris C., Janney P., 2020. Sources and effects of fluids in continental retrograde shear zones: Insights from the Kuckaus Mylonite Zone, Namibia. Geofluids, 2020(1), 3023268. https://doi.org/10.1155/2020/3023268.

Stepanov A.S., Allen C.M., Jiang S.-Y., Zhukova I.A., Duan D.-F., Wang L., 2024. Geochemistry of metasedimentary restitic rocks and implications for melting conditions and metal potential of crustal felsic magmas. Earth-Sci. Rev., 254, 104799. https://doi.org/10.1016/j.earscirev.2024.104799.

Taylor R.J.M., Kirkland C.L., Clark C., 2016. Accessories after the facts: Constraining the timing, duration and conditions of high-temperature metamorphic processes. Lithos, 264, 239–257. https://doi.org/10.1016/j.lithos.2016.09.004.

Tran N.N., 1998. Thermotectonic events from early Proterozoic to Miocene in the Indochina craton: implication of K–Ar ages in Vietnam. J. Asian Earth Sci., 16(5–6), 475–484. https://doi.org/10.1016/s0743-9547(98)00027-0.

Tran T.H., Zaw K., Halpin J.A., Manaka T., Meffre S., Lai C.K., Lee Y., Le V.H., Dinh S., 2014. The Tam Ky–Phuoc Son Shear Zone in central Vietnam: Tectonic and metallogenic implications. Gondwana Res., 26(1), 144–164. https://doi.org/10.1016/j.gr.2013.04.008.

Tran V.T., Faure M., Nguyen V.V., Bui H.H., Fyhn M.B.W., Nguyen T.Q., Lepvrier C., Thomsen T.B., Tani K., Charusiri P., 2020. Neoproterozoic to Early Triassic tectono-stratigraphic evolution of Indochinaand adjacent areas: A review with new data. J. Asian Earth Sci., 191, 104231. https://doi.org/10.1016/j.jseaes.2020.104231.

Tual L., Smit M.A., Kooijman E., Kielman-Schmitt M., Ratschbacher L., 2022. Garnet, zircon, and monazite age and ree signatures in (ultra) high-temperature and-pressure rocks: examples from the caledonides and the pamir. J. Metamorph. Geol., 40(8), 1321–1346. https://doi.org/10.1111/jmg.12667.

Usuki T., Lan C.Y., Yui T.F., Iizuka Y., Vu V.T., Tran T.A., Liou J.G., 2009. Early Paleozoic medium-pressure metamorphism in central Vietnam: evidence from SHRIMP U–Pb zircon ages. Geosci. J., 13, 245–256. https://doi.org/10.1007/s12303-009-0024-2.

Vernon R.H., 2011. Microstructures of melt-bearing regional metamorphic rocks. In Origin and Evolution of Precambrian High-Grade Gneiss Terranes (GSA Memoir 207). Geol. Soc. Am. https://doi.org/10.1130/2011.1207(01).

Wang S.F., Mo Y.S., Wang C., Ye P.S., 2016. Paleotethyan evolution of the Indochina Block as deduced from granites in northern Laos. Gondwana Res., 38, 183–196. https://doi.org/10.1016/j.gr.2015.11.011.

Wang Y.J., Wang Y.K., Qian X., Zhang Y.Z., Gan C.S., Senebouttalath V., Wang Y., 2020. Early Paleozoic subduction in the Indochina interior: Revealed by Ordo-Silurian mafic-intermediate igneous rocks in South Laos. Lithos, 362–363, 105488. https://doi.org/10.1016/j.lithos.2020.105488.

Wang Y., Zhang Y., Qian X., Wang Y., Cawood P.A., Gan C., Senebouttalath V., 2021. Early Paleozoic accretionary orogenesis in the northeastern Indochina and implications for the paleogeography of East Gondwana: constraints from igneous and sedimentary rocks. Lithos, 382, 105921. https://doi.org/10.1016/j.lithos.2020.105921.

Warren C.J., Greenwood L.V., Argles T.W., Roberts N.M.W., Parrish R.R., Harris N.B.W., 2019. Garnet–monazite rare earth element relationships in sub-solidus metapelites: a case study from Bhutan. Geol. Soc. Lond. Spec. Publ., 478, 145–166. https://doi.org/10.1144/sp478.1.

Weller O.M., Jackson S., Miller W.G., St-Onge M.R., Rayner N., 2020. Quantitative elemental mapping of granulite-facies monazite: Textural insights and implications for petrochronology. J. Metamorph. Geol., 38(8), 853–880. https://doi.org/10.1111/jmg.12552.

White R.W., Powell R., 2002. Melt loss and the preservation of granulite facies mineral assemblages. J. Metamorph. Geol., 20(7), 621–632. https://doi.org/10.1046/j.1525-1314.2002.00206_20_7.x.

Whitney D.L., Evans B.W., 2010. Abbreviations for names of rock-forming minerals. Am. Mineral., 95, 185–187. https://doi.org/10.2138/am.2010.3371.

Williams M.L., Jercinovic M.J., Harlov D.E., Budzyń B., Hetherington C.J., 2011. Resetting monazite ages during fluid-related alteration. Chem. Geol., 283(3–4), 218–225. https://doi.org/10.1016/j.chemgeo.2011.01.019.

Yakymchuk C., 2023. Prograde zircon growth in migmatites. J. Metamorph. Geol., 41(5), 719–743. https://doi.org/10.1111/jmg.12715.

Yakymchuk C., Brown M., 2019. Divergent behaviour of Th and U during anatexis: Implications for the thermal evolution of orogenic crust. J. Metamorph. Geol., 37(7), 899–916. https://doi.org/10.1111/jmg.12469.